Hurricane Andrew's Landfall in South Florida. Part II: Surface Wind Fields and Potential Real-Time Applications

MARK D. POWELL AND SAMUEL H. HOUSTON

Hurricane Research Division, NOAA/AOML, Miami, Florida

(Manuscript received 10 April 1995, in final form 8 February 1996)

ABSTRACT

All available wind data associated with Hurricane Andrew's passage were analyzed for periods corresponding to landfall south of Miami and emergence from southwest Florida. At landfall in southeast Florida, maximum sustained 1-min surface wind speeds V_{M1} reached just over 60 m s^{-1} in the northern eyewall over land; by the time Andrew exited the Florida peninsula, the peak value of V_{M1} over land decreased to 40–45 m s^{-1}. Radar reflectivity observations from Tampa and Melbourne could not support an obvious correlation of convective cell development with coastal convergence during landfall on the southeast coast. On the southwest coast, however, convective cell development in the southern eyewall was supported by a coastal convergence maximum. Comparison of the wind swath with two independent Fujita-scale damage maps indicated that peak swath speeds compared well with damage-derived speed equivalents in the worst damaged areas but were higher than equivalents in moderately damaged areas. Comparison of the analysis maximum wind swath with an engineering survey of damaged homes suggests that homes exposed to a wide range of wind directions while subjected to high wind speeds suffered the most damage. Potential real-time applications of wind field products include warning dissemination, emergency management, storm surge and wave forecasting, and wind engineering. Development of damage assessment models for disaster mitigation is addressed from the viewpoint of an electrical utility.

1. Introduction

Hurricane Andrew devastated a suburban and rural area south of Miami on 24 August 1992. The coastal ridge minimized inland penetration of the storm surge, and the rapid storm speed and small size contributed to relatively light (<200 mm) rainfall, which minimized flooding; hence, most of the damage to south Florida was caused by wind. The extent of Andrew's destruction was overwhelming for all concerned with hurricane preparedness, warning dissemination, emergency management, and disaster recovery. The combined economic and human impact of landfall ranks Andrew as the costliest natural disaster in the history of the United States. The confusion brought on by damage to the communication, transportation, and electrical utility infrastructure made it very difficult to determine which areas received the most damage.

This study examines the structure of the wind field at landfall, its relationship to the damage field, and the changes that occurred to the wind and reflectivity fields by the time Andrew exited southwest Florida for the Gulf of Mexico. This paper also explores meteorological products constructed from Andrew's wind field that have potential for real-time use in warning dissemination and emergency management, improved wave and storm surge model simulations, and damage assessment. The reader is referred to Mayfield et al. (1994) for a comprehensive discussion of Hurricane Andrew's synoptic history and storm track.

Corresponding author address: Dr. Mark D. Powell, Hurricane Research Division, NOAA/AOML, 4301 Rickenbacker Cswy., Miami, FL 33149.
E-mail: powell@aoml.noaa.gov

2. Procedure

a. Data

Data sources and methods used to create a comprehensive surface wind dataset conforming to a common framework for exposure (marine or open terrain over land), height (10 m), and averaging time (maximum 1-min sustained wind speed, V_{M1}) are discussed in the companion paper Powell et al. (1996, hereafter Part I). The errors in using these procedures to estimate V_{M1} from conventional observations are on the order of 10%. Differences between aircraft measurements (adjusted from 70.0 kPa to the surface) and nearby surface measurements of V_{M1} are on the order of ±20% but may be much less due to the difficulty of finding valid comparisons where there are large radial gradients of wind speed.

b. Analysis method

Analysis of the input wind data from Hurricane Andrew is based upon the Spectral Application of Finite-

Element Representation (SAFER) method (Ooyama 1987; Lord and Franklin 1987; DeMaria et al. 1992; Franklin et al. 1993). In SAFER, cubic B splines minimize in a least squares sense the deviations between the input observations and the analysis. One advantage of this type of analysis is that the wind is defined continuously in the domain, not just at the locations of the grid points. The spline fit is controlled by a derivative constraint that acts as a mesoscale low-pass spatial filter. A nested version of SAFER allows the specification of different filters for each nest that depend on the scale of the features to be resolved. The nest geometries for the SAFER analyses on each coast are shown in Fig. 1. The innermost mesh focuses on the wind structure of the eyewall including the magnitude of the highest wind and its distance from the storm center, mesh 2 covers the extent of hurricane force winds, and meshes 3–5 convey the extent of greater than 25 m s^{-1} and greater than gale (18 m s^{-1}) force winds over the ocean and land. Hurricane forecasters enter these quantities as standard input to warnings and watches issued in marine and public advisories. Mesh 5 is the same for each analysis.

The mesoscale filter reduces the amplitude of wind maxima present in the input data. As described below, these amplitudes were restored to reduce possible underestimation of winds in the analysis. Powell et al. (1991) analyzed the surface wind field of Hurricane Hugo using an unnested version of SAFER, but did not use the input data framework defined in Part I of this paper, nor did they attempt to restore amplitudes smoothed by the mesoscale filter. At any point in the wind analysis domain a timescale is defined as

$$T_m = \frac{2\lambda}{V_{\text{meso}}}, \tag{1}$$

where λ is the analysis spatial filter wavelength in meters (corresponding to the half-power point of the filter response function) and V_{meso} is the mesoscale analysis wind speed. The mesoscale wind may be converted to a maximum t-period mean wind that may have occurred over T_m by applying an appropriate gust factor. For hurricane warning and advisory applications, the maximum sustained surface wind V_{M1} (1-min average at 10 m) has been adopted by the National Hurricane Center (NHC). The amplitude of the mesoscale analysis wind data was restored by applying the 1-min gust factor (from Fig. 9 of Part I) consistent with T_m:

$$V_{\text{M1}} = V_{\text{meso}} G_{60,T_m}. \tag{2}$$

One way to visualize V_{M1} is to consider a dense network of anemometers measuring winds in a stationary hurricane that maintains the same intensity for 1 h. If the highest 1-min average wind speeds over the hour were saved for each station and contoured, the result would correspond to a maximum sustained wind field. The advantage of this technique for mesoscale objective analysis is that all winds are associated with the same averaging time; analysis winds are readily verified if independent continuous measurements are available from platforms. In high wind conditions, the timescale given by (1) may be considerably smaller than the 60-min reference used in many gust factor relationships (e.g., Krayer and Marshall 1992). For high-resolution hurricane wind field analyses near the core of the storm, typical values of T_m range from 10 to 30 min; lower-resolution analyses farther from the core or in lower wind strength areas would have larger T_m values, comparable to 60 min or more. For Andrew's landfall analysis, deviations of V_{M1} from 128 input observations in mesh 1 suggest that the SAFER technique combined with the amplitude restoration method overestimates the input observations by 1.3 m s^{-1}, with a root-mean-square (rms) difference of $\pm$1.3 m s^{-1} compared with a mean underestimate of 2.1 m s^{-1} and rms of $\pm$2.8 m s^{-1} if only the mesoscale analysis (without amplitude restoration) is considered.

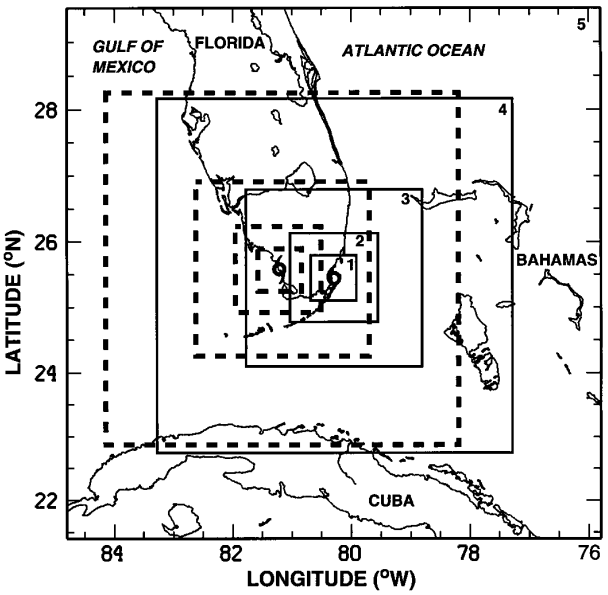

FIG. 1. Nested analysis mesh geometry. Solid lines pertain to landfall analyses on the southeast coast; dashed lines refer to analyses for the southwest coast.

c. Analysis time periods

The track of Andrew's wind center is displayed in Fig. 2 together with the time periods chosen for the analysis and the maximum flight-level winds and central sea level pressures (SLP) measured during each period. Additional information on Hurricane Andrew's development and history are available in Mayfield et al. (1994). Plots of flight-level winds in the eye and public reports of calm surface winds and their duration in the vicinity of Homestead were used to construct a

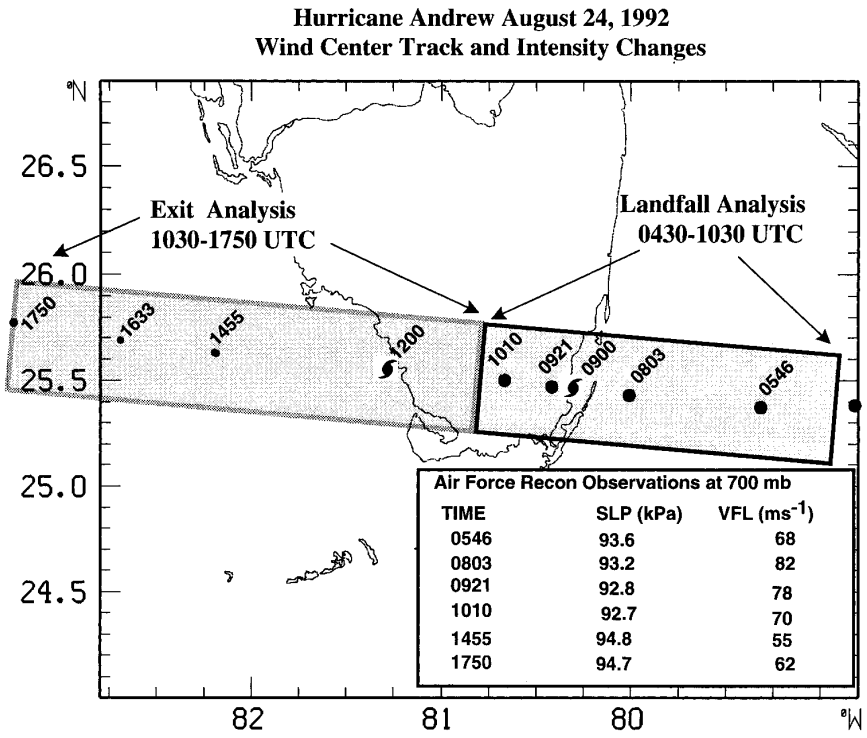

FIG. 2. The track of Andrew's wind center and intensity changes as indicated by air force reconnaissance flight-level measurements of wind speed (m s^{-1}) and calculated minimum central sea level pressure (kPa). Boxed area to the right represents time period of the southeast coast landfall analysis (0430–1030 UTC) and area to the left indicates time period of the exit analysis for the southwest coast (1030–1750 UTC).

track of the circulation center. Center fixes over southwest Florida were estimated from radar reflectivity data where surface and flight-level wind observations were unavailable. Andrew's circulation center made landfall at 0900 UTC. The period from 0430 to 1030 UTC was chosen to depict the wind field during Andrew's landfall in southeast Florida, including surface observations for 0545–1030 UTC and surface-adjusted aircraft observations from 0430 to 1030 UTC. Shorter time periods excluded many observations and resulted in large data-sparse areas. As shown in Fig. 2, the SLP derived from flight-level measurements decreased from 93.6 to 92.7 kPa from 0546 to 1010 UTC and then increased to 92.7 kPa by 1010 UTC. Minimum SLP measured at the surface (92.2 kPa) occurred between 0900 and 0915 UTC a few kilometers northwest of the circulation center (see Fig. 10 of Part I). Maximum 1-min flight-level wind speeds in the northern eyewall increased from 68 m s^{-1} to a maximum of 82 m s^{-1} at 0803 UTC and then decreased to 70 m s^{-1} by 1010 UTC. Maximum winds were consistently highest in the northern eyewall throughout Andrew's approach, landfall, and exit from south Florida.

The analyses for Andrew's exit from southwest Florida include the period from 1030 to 1750 UTC. Unfortunately, there was no additional aircraft reconnaissance coverage of Andrew while the center was over land; flight-level observations resumed at 1430 UTC, about 2.5 h after the center emerged over the Gulf of Mexico. After 1010, Andrew's SLP increased 2.1 kPa, and maximum 1-min flight-level wind speeds on the north side weakened to 55 m s^{-1} by the time of the first pass of the U.S. Air Force Reserves reconnaissance aircraft off the southwest coast at 1450 UTC. By 1800 UTC, Andrew's flight-level winds strengthened to 62 m s^{-1} on the north side of the eyewall, while SLP remained approximately constant. Andrew's SLP began to deepen later, with substantial decreases at 1920 UTC (0.15 kPa) and 2100 UTC (0.3 kPa). It is possible that Andrew may have been weaker during the 4-h period of no aircraft coverage from 1030 to 1430; the center would have been over open water for about 2.5 h by 1430 UTC. No surface data were available to document the storm intensity during this period, but the first few passes of the air force reconnaissance aircraft indicate very slow intensification consistent with the large portion of the circulation still over land. Although most of the core flight-level data were collected from 1430 to 1750 UTC, the analysis for Andrew's exit from south Florida was positioned relative to geography corresponding to the time (1200 UTC) the circulation center was just beginning to emerge from land.

3. Wind structure at landfall in southeast Florida

a. Surface winds

Separate mesoscale analyses of mesh 1 were completed for datasets corresponding to open terrain over land (Fig. 3a) and marine (Fig. 3b) exposures, respectively (exposures are described in Part I). Geography is plotted for the position of the storm center at landfall (0900 UTC). After restoring the wind speed amplitudes, the land and marine parts of the analysis are merged together at the coastline to form the V_{M1} wind field at landfall (Fig. 3c). The discontinuity at the coastline corresponds to a transition zone where oceanic flow adjusts to land, and vice versa. The actual width of the transition zone is unknown. While models described in Part I suggest transition length scales of 1–3 km, adjustment procedures applied to Low-Level Windshear Alert System data described in Part I indicate that equilibrium flow may not be reached even after 30 km. Since all input data over land were converted to open-terrain exposure, the winds presented here are higher than those that applied to the actual suburban terrain of south Florida. Methods described in Part I are available to convert open-terrain winds to those that might have occurred at any given exposure.

According to the analysis in Fig. 3c, Andrew's maximum winds were in the northern eyewall near Perrine where onshore flow reached a maximum of 66 m s^{-1} on the coast and then decreased to 62 m s^{-1} just inland. The difference between land and marine winds in the vicinity of the eyewall are relatively small due to comparable roughness lengths for marine and open terrain in high winds, as discussed in Part I. Radar reflectivity features associated with the eyewall at landfall, as observed from the Melbourne WSR-88D radar (Fig. 4a), are plotted on the same scale as Fig. 3c. In general, the highest winds are found slightly inward from the maximum reflectivities in the eyewall. The wind maximum on the south side of the eyewall may be associated with a downdraft produced by an intense convective cell detected by the Miami (MIA) WSR-57 radar data (not shown) from 0821 to 0833 UTC near the vessel *Mara Cu* (see Part I) just to the north of Key Largo. This type of feature was also present at 0901 UTC based on the reflectivity measurements in Fig. 4a. The 55 m s^{-1} isotach extends to the southeast of the eyewall in both land and sea analyses and is consistent with eyewitness reports that the strongest winds in the Homestead area blew from the south from 0950 to 1010 UTC. However, the location (see Fig. 10 of Part I) of the onset of strong south winds at Homestead (0945 UTC), Florida City (0948 UTC), and Leisure City (0945 UTC) was closer to the circulation center than depicted by the surface-adjusted aircraft winds.

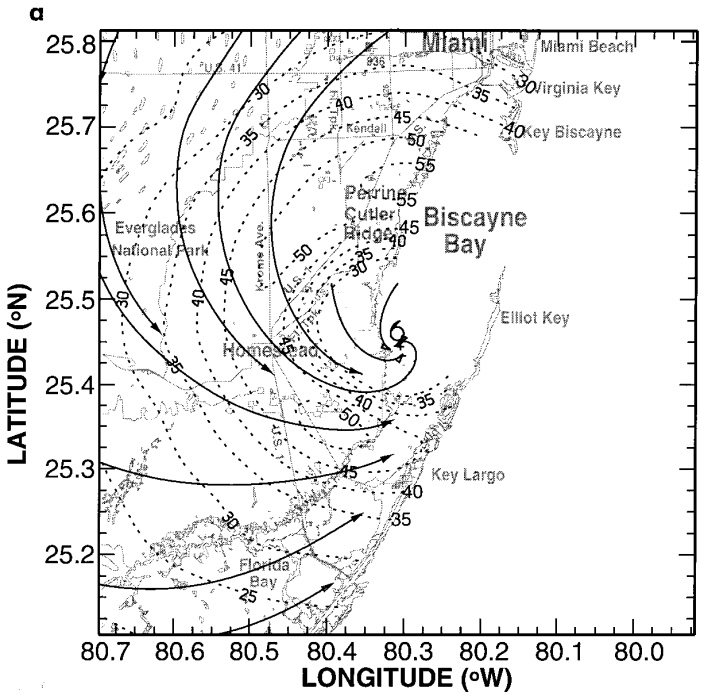

FIG. 3. Analyses of Hurricane Andrew's landfall for 0900 UTC 24 August 1992: (a) mesoscale analysis (m s^{-1}) for open terrain over land conditions, (b) mesoscale analysis (m s^{-1}) for oceanic conditions, and (c) merged V_{M1} (m s^{-1}) analysis for mesh 1 created from (3a) and (3b), but with amplitudes restored.

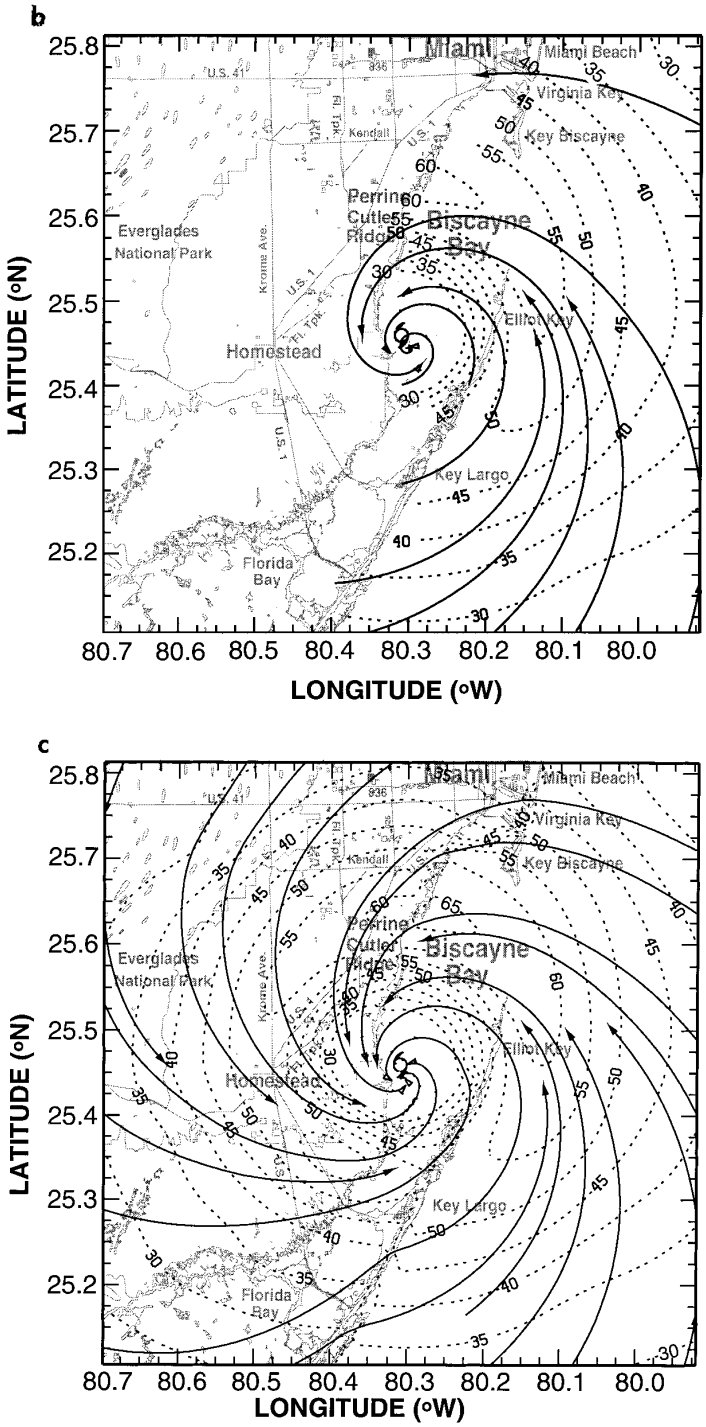

FIG. 3. (*Continued*)

The portion of the wind field (and the derived divergence and vorticity fields described below) depicted within the eye is somewhat speculative since no surface wind measurements were available within the eye to validate surface adjusted aircraft observations. Eyewitness reports of calm in Homestead (0929–0935 UTC) compare well with the flight-level circulation center, but the minimum surface pressure in Andrew (see Fig. 10 of Part I) was located about halfway between the eyewall and the cir-

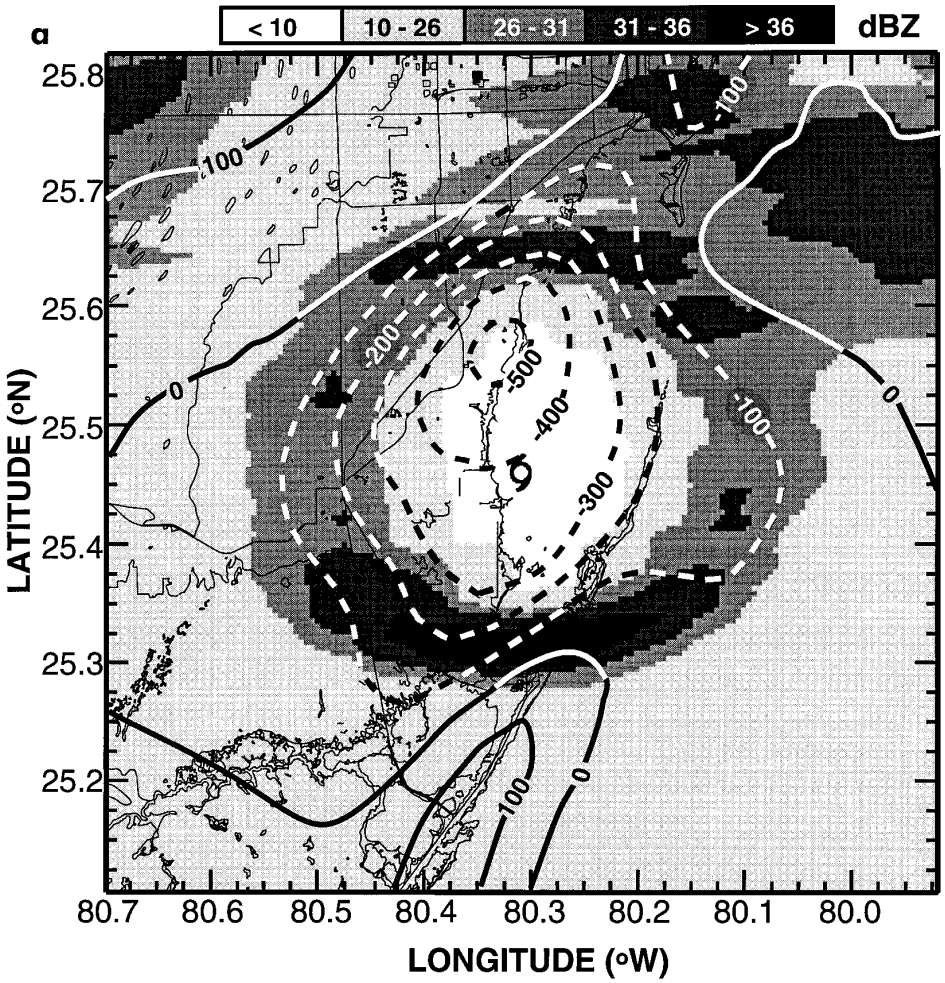

FIG. 4. As in Fig. 3 but for (a) radar imagery for mesh 1 from Melbourne WSR-88D at 0901 UTC with divergence ($\times 10^{-5}$ s^{-1}) contours (dashed) from mesoscale merged wind analysis and (b) vorticity ($\times 10^{-5}$ s^{-1}) contours (dashed) from mesoscale merged wind analysis.

culation center and may have been associated with a ''warm spot'' detected by satellite (Willoughby and Black 1996).

b. Kinematics and radar reflectivity

Time-lapse animations constructed from radar images in past hurricanes have suggested that reflectivity cell development is most likely in areas of enhanced convergence where onshore flow crosses the coast (Parrish et al. 1982). In a cylindrical coordinate system, divergence (Div) is

$$\text{Div} = \partial V_\theta / R\partial\theta + V_R/R + \partial V_R/\partial R, \qquad (3)$$

where θ is the azimuthal coordinate, R is radial coordinate, and V_θ and V_R are the tangential and radial components of the wind velocity. The divergence computed from a merged version of the mesoscale analyses (Fig. 4a) shows convergence extending along the coastline to the north of the center and divergence to the south of the center where the flow accelerates offshore. The main effect of terrain on the wind field is an increase (decrease) in convergence through a negative (positive) $\partial V_\theta/R\partial\theta$ and increased (decreased) negative V_R/R where the flow impinges on (exits from) the coastline. Maximum convergence of 5×10^{-3} s^{-1} is on the inner edge of the northern eyewall. From outer radii to near the radius of maximum wind (R_{MW}), the $\partial V_R/\partial R$ term is positive; it becomes negative within the R_{MW} contributing to the maximum in the eye. Although there is still some question as to the details of the surface wind pattern within the eye of Andrew, inflow and attendant convergence at low levels within the eye is a common feature of tropical cyclones and is often evident as a swirl of low clouds partially obscuring the sea surface beneath a clear area suggestive of middle- and upper-level subsidence. Above the

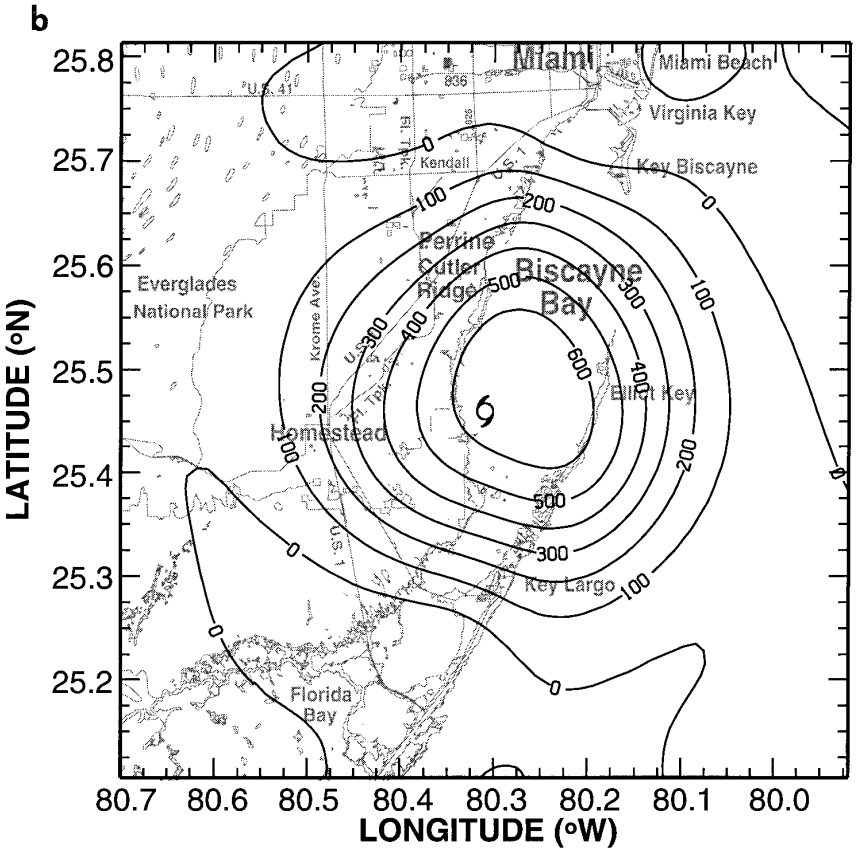

FIG. 4. (*Continued*)

boundary layer ($>1.0-1.5$ km), at or slightly inward of the R_{MW}, inflow typically vanishes or changes to weak outflow. This location is consistent with the position of the mesoscale eyewall updraft. Observations of low-level moisture and shallow ascent in the eyes of tropical cyclones have been documented by dropsonde observations (e.g., Jordan 1961; Franklin et al. 1988; Willoughby et al. 1989) and photographs of the eye taken from satellites and high altitude aircraft (e.g., Fletcher et al. 1961; Simpson and Riehl 1981; Anthes 1982).

Comparisons of time-lapse radar animations of reflectivity distributions constructed from MIA and Tampa (TBW) WSR-57 radars, and the Melbourne (MLB) WSR-88D radar (Dodge et al. 1993; Willoughby and Black 1996) provide conflicting evidence of the relationship between convergence and enhanced convective cell development. The radars have 10-cm wavelengths, which should limit attenuation problems. For a 0.5° elevation angle, the height of the center of the beam over Miami is 8.2 km for TBW and 6.7 km for MLB. Recording intervals were 1 min at MIA and TBW, and 5 min at MLB. Reflectivity values for TBW were adjusted to agree with MIA observations before the MIA radar went out of service at 0841 UTC. The closest radar (MLB) agreed well with the MIA radar (in terms of reflectivity distribution in the eyewall) before the outage; afterward, it suggests no apparent relationship between the coastline and the location of intense eyewall cells during landfall. TBW was farther from the storm but gives the impression of a convective life cycle with cells forming on the north side of the eyewall, maturing on the west and south sides, and decaying on the east side during the southeast coast landfall. The lack of agreement may be related to the different beam volumes; MLB has a 1° beam compared with 2° for TBW. The possibility of the beam overshooting the important convective features exists because the bottom of the beam at MLB (4.4 km) is coincident with the typical melting-layer altitude in hurricanes, while at TBW the lower part of the beam is 2.9 km. TBW includes the entire MLB beam volume but may be affected more by the amount of liquid water at the bottom of the volume. Hence, MLB may have missed the initial development of cells (with liquid water concentrated lower) and only sampled mature cells. On the other hand, Andrew's eye was very warm (15°–17°C at 70.0 kPa), and the eyewall was intense enough that much liquid was also present within MLB's beam volume.

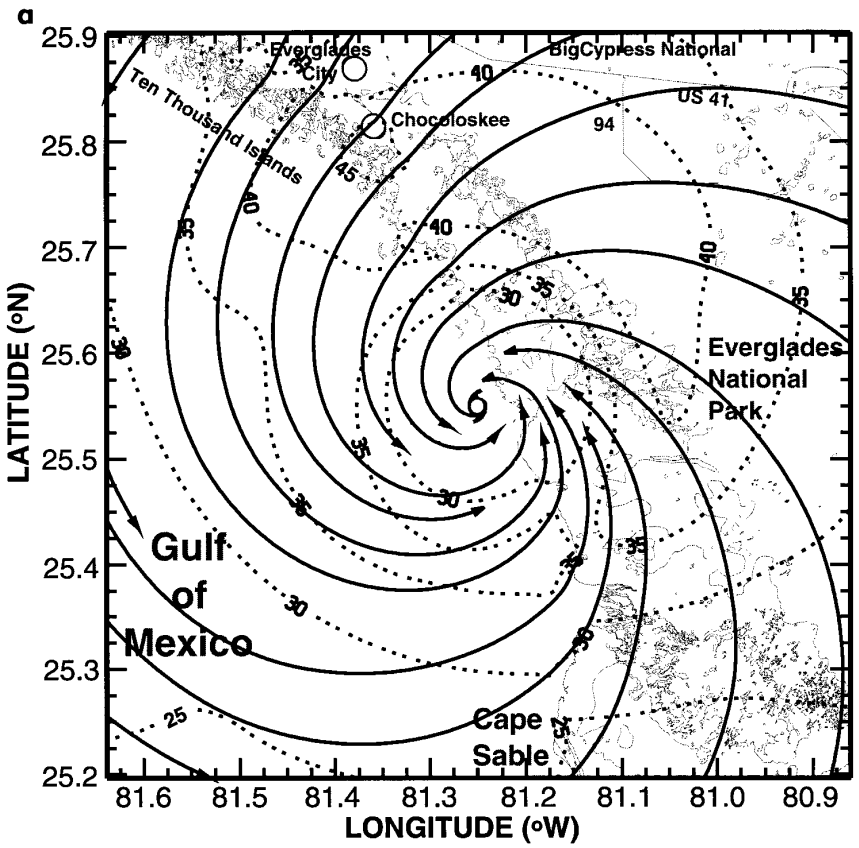

FIG. 5. Hurricane Andrew upon exit from southwest Florida: (a) as in Fig. 3c but for southwest coast at 1200 UTC, (b) as in Fig. 4a but for Tampa WSR-57 at 1151 UTC.

c. Vorticity distribution and speculation on damage streaks

The distribution of the vertical component of vorticity (Fig. 4b) computed from merged mesoscale analyses indicates a peak of $6 \times 10^{-3}\ s^{-1}$ in the eye with values of $3-4 \times 10^{-3}\ s^{-1}$ in the eyewall. Rotational flow is limited to the core region within 40 km of the storm center; the anticyclonic shear component cancels the curvature component outside the core. The analysis in Fig. 4b indicates peak vorticity in the eye. However, the actual location of the vorticity maximum may not have been resolved by the observations; Willoughby and Black (1996) suggest that the surface pressure and vorticity centers may have been located adjacent to the northern eyewall in concert with the formation of a convective mesovortex.

Vorticity of this magnitude may be associated with observed ''streaks'' of damage documented in Hurricane Andrew by Fujita (1992a) and Wakimoto and Black (1993), and attributed to ''miniswirls'' or small-scale tornadoes. The worst damage streaks occurred in Naranja Lakes (for location see Fig. 10 of Part I) and Cutler Ridge, resulting in four deaths. Damage streaks at Naranja Lakes occurred near the western eyewall (at the R_{MW}, see Part I) and eastern eyewall (data are insufficient to determine streak location relative to the eastern R_{MW}); streaks in Cutler Ridge were on the inner side of the R_{MW} in the northern and northeastern eyewall. A tendency for the streaks to occur on the inner side of the R_{MW} would suggest that eyewall-scale vorticity may be important. Unfortunately, the space and time resolution of the input data described here cannot adequately sample such small-scale features, nor could an analysis of this scale resolve them. We can, however, invoke scale arguments to speculate on generation mechanisms.

Length scales of the damage streaks (100–200 m) and representative sustained wind values of 40–60 $m\ s^{-1}$ in Fig. 3c indicate that timescales of the streak-producing features are 3–5 s. The small time and space scales of these features suggest a turbulent or small convective-scale generation mechanism. Flight-level measurements of vertical motions in hurricanes indicate that the strongest updraft and downdraft cores have radial scales on the order of 5 km (Jorgensen et al. 1985; R. Black, HRD, 1993, personal communication). Individual downdraft gusts

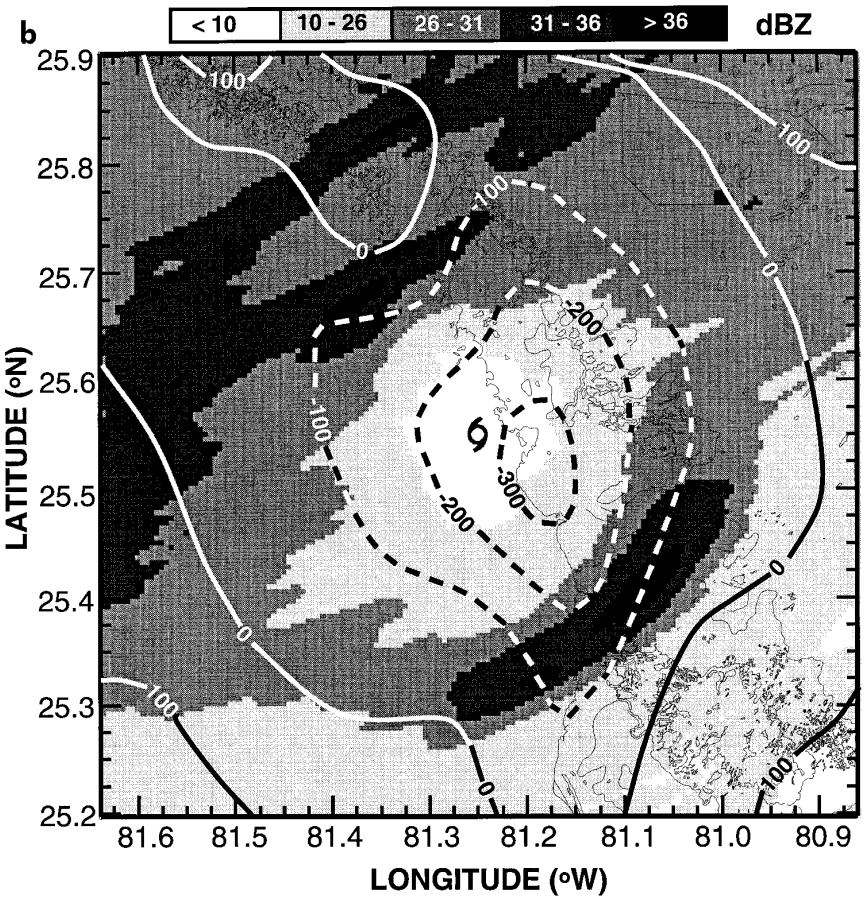

FIG. 5. (*Continued*)

of this scale would be too large to be related to the streaks, but the shear generated on the edge of a gust associated with a downdraft could be concentrated over a small area. A horizontal wind shear of 15 m s^{-1} over a distance of 100–200 m is conceivable between the downdraft gust (30% greater than V_{M1}) and adjacent flow. Hence, a large vertical vorticity component of order $1-2 \times 10^{-1}$ s^{-1} can be produced in a very small area on the inner edge of the gust where eyewall-scale vorticity is already strong. The strong convergence at the head of the downdraft could force adjacent air to ascend, causing the vorticity to stretch in a manner similar to gustnadoes embedded within gust fronts of mesocyclones (Forbes and Wakimoto 1983; Wilson 1986). It is also conceivable that strong horizontal shear on each side of the downdraft could induce the creation of a vortex pair, cyclonic on the left and anticyclonic on the right (looking downwind). Additional mechanisms to create, and maintain, a vortex of sufficient rotation speed to produce a substantial increase in already strong sustained winds are not clear, but it is apparent that the timescales are very short. Current volume scan strategies (5–6 min) and beam geometry limitations of the WSR-88D radar will not detect the relatively short life cycles and small scales associated with damage streak vortices.

4. Changes in the wind field after landfall

a. Southwest Florida

The distribution of V_{M1} (mesh 1) for Andrew's exit from southwest Florida at 1200 UTC (Fig. 5a) contains maximum winds in the northern eyewall of 44 m s^{-1} a few kilometers south of Chokoloskee. An unusual feature of the wind field at this time is the 29-km R_{MW} that was maintained on the north side compared to the 15–20-km R_{MW} on the other sides. The wind maximum on the north side of the storm broadened and moved outward in association with a rainband about 12 km north of the northern eyewall shown in the reflectivity distribution at 1151 UTC from the Tampa WSR-57 radar (Fig. 5b). The eye diameter is difficult to determine, but comparisons with images from the Tampa radar at 0900 UTC (not shown) do not show any obvious

changes. Convergence (Fig. 5b) has decreased compared with convergence in the southeast coast composite, and peak values have shifted to the southeast of the center along the coastline. A small divergence region lies to the northwest of the center where flow begins to accelerate offshore, as shown by the 45 m s^{-1} isotach on the coastline and the expanded area of greater than 35 m s^{-1} and greater than 40 m s^{-1} isotachs. Time-lapse animations of radar reflectivity images (Dodge et al. 1993) indicate that active cell development took place in the region of onshore flow just north of Cape Sable and at Everglades National Park to the southeast of the center; images from MLB corroborated this impression.

b. Intensity change over south Florida

Comparison of the southeast and southwest coast landfall wind fields and examination of radial profiles of flight-level wind speed and D value (not shown) indicate that the decay of Andrew's wind field occurred primarily within 50–60 km of the circulation center, hereafter referred to as the ''core.'' Outside the core, the winds on the north and south sides changed very little relative to the southeast coast landfall wind field. Comparisons of landfall and postlandfall analyses of Hurricanes Alicia (Powell 1987) and Hugo (Powell et al. 1991) (5 and 3 h after landfall, respectively) also imply that most of the wind field decay occurs in the core region. Tropical cyclone landfall simulations (Tuleya and Kurihara 1978; Tuleya et al. 1984) also suggest primary weakening of the wind and pressure field near the storm center, with indications of kinetic energy increases and a broadening circulation at outer radii. Decay within the core does not appear to be related to concentric eyewall development. A concentric eyewall cycle described by Willoughby and Black (1996) affected Andrew earlier in the Bahamas. While approaching south Florida, Andrew intensified dramatically with the (formerly outer) eyewall diameter shrinking continuously through landfall. Afterward, time-lapse radar animations and flight-level wind profiles indicate no clearly defined outer concentric eyewall feature; the intensity cycle ceased due to processes associated with landfall.

To depict the change in Andrew's peak winds while passing across Florida, analyses of V_{M1} (marine and land exposures) for the southeast and southwest coasts were advected at 1-min intervals along the storm track for mesh 4. The sequence of advected analyses included the southeast coast analysis (0300–0930 UTC), an interpolated field (0930–1030 UTC), and the southwest coast analysis (1030–1755 UTC). The highest wind at each 5.75-km-spaced grid point was recorded and contoured to construct a swath (Fig. 6) of the highest V_{M1} winds that may have occurred during Andrew's passage across Florida. The swaths for marine and open-terrain land exposures are merged at the coastline similar to Figs. 3c and 5a. To the north of the center, the magnitude of land–sea discontinuity in the onshore flow increases with distance from the storm because differences between open-terrain and marine roughness increase with decreasing wind speed. The wind swath suggests that greater than 50 m s^{-1} winds extended more than halfway across the state; however, without continuous wind measurements in the eyewall between 1030 and 1430 UTC, it is difficult to determine how far inland the maximum winds actually penetrated. As discussed above, Andrew decayed most rapidly in the vicinity of the core; after landfall, very little wind speed change is observed in areas having V_{M1} less than 40 m s^{-1} on the north side and less than 33 m s^{-1} on the south side.

Minimum pressures measured in the eye changed very little during landfall based on flight-level passes from 0920 to 1010 UTC, although peak winds in the northern eyewall decreased with each successive pass. Numerous public reports of SLP minima in the eye were analyzed by the NHC (Mayfield et al. 1994; Rappaport 1994). The lowest SLP measured in Andrew at landfall (92.2 kPa) was observed in the northern part of the eye from 0900 to 0915 UTC, shortly after the circulation center moved ashore. The differences between this observation and others within the eye (±.5 kPa) may have been within the accuracy of instruments, but the timing coupled with the lack of an im-

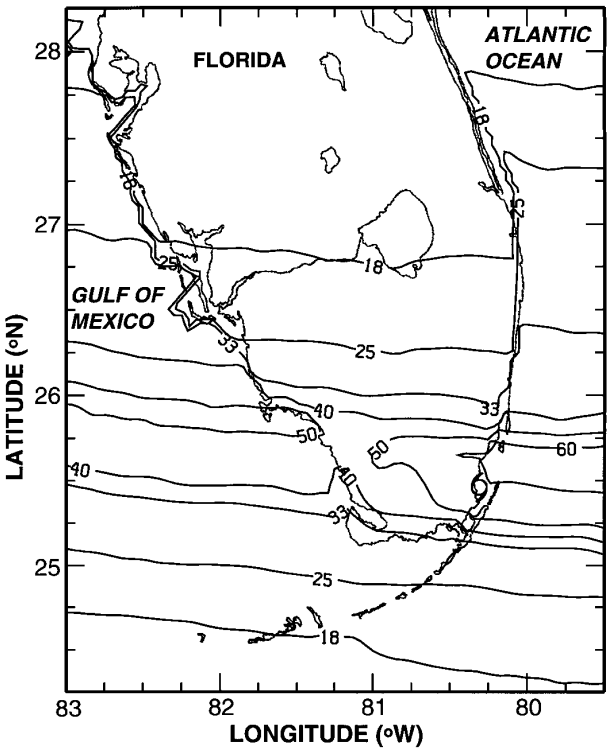

FIG. 6. The V_{M1} swath map for mesh 4. Contours represent an estimate of the maximum V_{M1} experienced during the storm.

mediate increase in flight-level pressures and the storm track over the Everglades has led to speculation that Andrew may have intensified (Wakimoto and Black 1993) or maintained its intensity while passing across Florida. This speculation is not supported by the wind analyses, subsequent flight-level measurements of equivalent potential temperature and pressure, or recent simulation experiments. By increasing surface roughness and maintaining an oceanic evaporation source over land, Tuleya and Kurihara (1978) simulated hurricanes that continued to intensify after landfall. Recently, Tuleya (1994) conducted simulations with a much more realistic model that contained a bulk surface temperature prediction scheme. He concluded that finite subsurface thermal properties over land (soil heat capacity and conductivity) suppressed potential evaporation and resulted in lower surface temperatures and higher SLP.

Despite the fact that Andrew's eyewall transited the relatively moist Everglades, peak winds decreased by about 33%, and SLP increased by 1.9 kPa over a period of 6 h. These changes are not surprising in comparison with Hurricane Donna in 1960 (Miller 1964), which paralleled the southwest coast moving north-northwest from Florida Bay and then north through Naples and Fort Myers over a 10-h period. Miller found that Donna weakened due to loss of the oceanic moisture and heat source even though much of the circulation was over relatively moist land. While just offshore from southwest Florida, Donna's SLP increased 1.9 kPa, the sustained wind speed decreased by 28%, and the maximum equivalent potential temperature θ_E in the eye decreased from 371 to 359 K from 0900 to 1900 UTC 10 September 1960. These changes occurred despite nearly half of the circulation being over the Everglades, Big Cypress, and Corkscrew Swamp areas of southwest Florida. Flight-level temperature data from the 1450 UTC pass through Andrew indicated that peak θ_E in the eye had dropped to 357 K from 366 K at landfall on the southeast coast. Application of the empirical relationship, $\Delta p \approx -2.5\,\Delta\theta_E$, of Malkus and Riehl (1960) to Andrew's passage across Florida results in a sea level pressure increase of 2.4 kPa, about .5 kPa more than observed. Apparently, Andrew underwent a period of very rapid intensification while approaching Florida; landfall initiated the decay process, manifested immediately as a decrease in the peak winds of the storm core.

5. Relationship of maximum winds to observed damage

Is damage to structures and vegetation controlled only by the maximum wind speed attained during the storm? Comparisons of the wind field with damage surveys suggest that additional factors may be relevant. Meteorological surveys of damage debris patterns are conducted to identify mesoscale or smaller-scale wind features associated with a storm and to estimate winds where no observations are available. Engineering damage surveys help determine modes of failure and whether design winds for a particular type of structure or building component may have been exceeded. If we are to learn from wind disasters, meteorologists and engineers must cooperate and interact during poststorm damage surveys and wind field analyses. Numerous surveys of Andrew's damage were produced after the storm. Since similar damage surveys are conducted routinely after major severe weather disasters, it is important that surveys be examined for consistency and evaluated relative to careful poststorm wind field analyses representing a common exposure and averaging time framework.

a. Swath of maximum winds

A wind swath map was constructed for mesh 1 at the time of landfall (Fig. 7) by advecting the marine and open-terrain land analyses along the storm track. Except for the coastline, isotachs in Fig. 7 are straight lines because the intensity at landfall depicted in Fig. 3c was assumed to apply to the entire time required for the eyewall to traverse the geography shown. The swath shows that the maximum V_{M1} of 60–62 m s^{-1} from the northern eyewall passed through the Perrine area and very strong winds of in excess of 55 m s^{-1} extended from Kendall to several kilometers south of Homestead. Wind directions associated with the strongest analysis wind speeds (shown as arrows in Fig. 7) were northeast in Kendall and Perrine, shifting to east in Cutler Ridge, and southeast at Naranja Lakes (see Part I for locations). From Homestead south, the strongest winds were associated with the western and southern parts of the eyewall with wind directions from the northwest and then west just south of Homestead (at Florida City). The secondary maximum of speeds greater than 55 m s^{-1} was associated with a wind maximum on the south side of the eyewall. Three of the best-known damage surveys (Fujita 1992a; Wakimoto and Black 1993, hereafter WB; Crandell 1993) are summarized in Fig. 8 on the same scale as the wind field analyses.

b. Fujita's damage analysis

The Fujita (1992a) meteorological damage debris analysis was conducted with high-resolution aerial photographs and ground visits. The techniques for visual damage surveys and the equivalent wind speeds for each damage scale category pioneered by Fujita are described in Fujita (1971). Originally, the Fujita damage scale was defined with an uppercase F, which was valid for damage to wood frame construction. Comparisons to mean surface wind analyses in Hurricane Frederic (Powell 1982) suggested that the F-2 range mean wind equivalents overestimated analysis winds

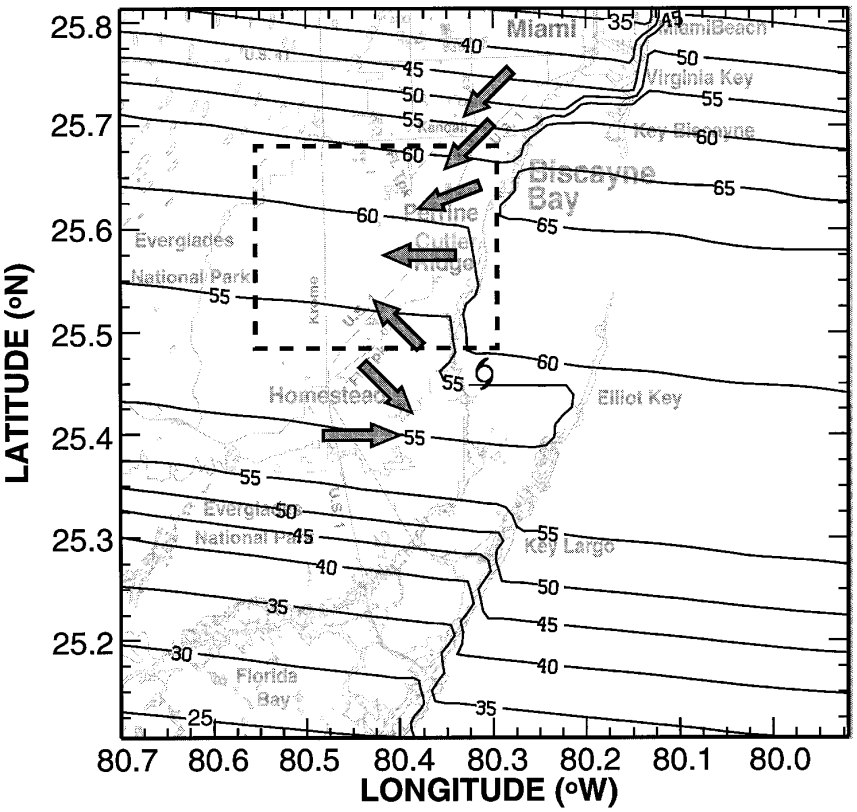

FIG. 7. The V_{M1} swath map for mesh 1 on the southeast coast. Arrows refer to direction associated with maximum V_{M1}. Inset box refers to area displayed in Fig. 14.

by 10%–50%. Limitations of the Fujita scale survey technique have been discussed by Minor et al. (1977) and Doswell and Burgess (1988), and accuracy of the method is estimated at ± one F number. The primary criticism of the technique was the difficulty of taking into account the wind resistance of the structures contributing to the damage field; construction and vegetation characteristics can vary greatly over a damaged area.

To allow correction of the damage scale for the strength of the damaged structure, Fujita (1992b) defined a lowercase f scale, which was used in his analysis of Hurricane Andrew. Unfortunately, Fujita (1992a) did not publish the uppercase F-scale wind speed equivalents corresponding to the revised lowercase f-scale damage numbers for the Andrew survey, so we cannot assign wind speeds to his f-scale estimates. Fujita's damage map of Hurricane Andrew identified six primary damage areas (Fig. 8): 1–3 from the ''first wind'' produced by the western part of the eyewall and 4–6 from the ''second wind'' on the northeast, east, and south portions of the eyewall. Point observations of f-3 intensity were found in areas 1, 4, and 6, with the highest density of f-2 and f-3 observations in area 4. Roughly 75% of area 4 and 40% of area 3 coincide with 60–62 m s^{-1} peak V_{M1} winds according to Fig. 7, and peak V_{M1} of 50–60 m s^{-1} were analyzed in the remaining areas.

c. *Wakimoto and Black's damage analysis*

The WB survey was conducted independently by scientists originally trained by Fujita, using site visits and a different set of photographs taken from a small aircraft. In this case, a lowercase f scale was defined by WB (and published in the poster they produced, which is available from NOAA/HRD, 4301 Rickenbacker Causeway, Miami, FL 33149) for the concrete block and stucco (cbs) construction vernacular of south Florida. Lowercase f-scale contours from WB are reproduced in Fig. 8. The conversion to the uppercase F scale (valid for wood frame construction) and the wind speed equivalents are shown by the key in Fig. 8. The maximum 2-s wind gust in WB's conversion table has been converted to V_{M1} [by applying a gust factor, $G_{2,60}$, of 1.3 from Powell et al. (1991)] in Fig. 8. The WB survey identified two f-3 locations that coincided with Fujita's f-3 values in the vicinity of Naranja Lakes and Cutler Ridge; these sites were associated with maximum sustained winds of 55–60 m s^{-1} (Fig. 7). Even

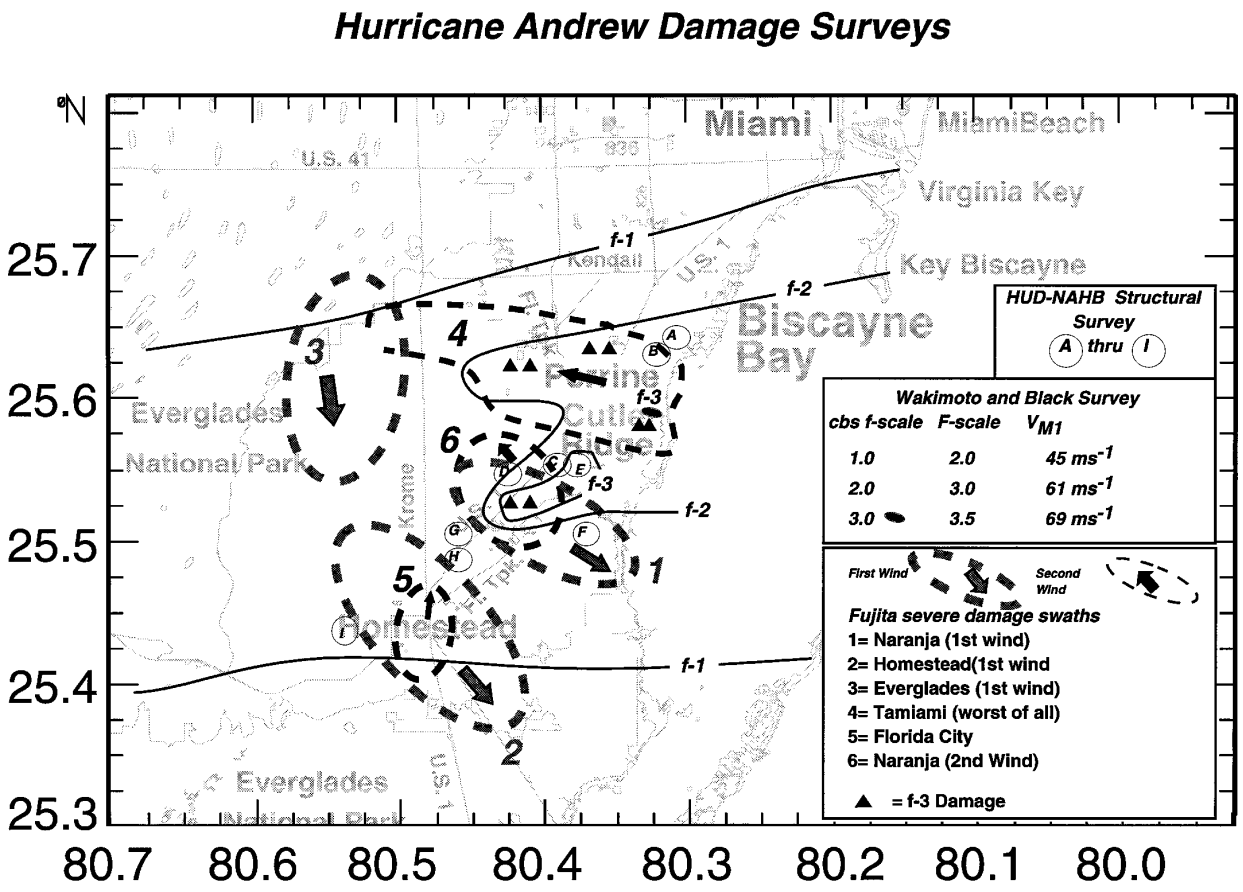

FIG. 8. Damage survey map showing areas A–I analyzed by Crandell (1993), damage areas 1–6 defined by Fujita (1992a), and f-scale contours from Wakimoto and Black (1993).

though similar techniques were employed, the f-scale surveys disagreed in some locations. Additional f-3 locations found by Fujita in area 4 and f-2 sites found in areas 2, 3, and the western part of area 4 were not identified by WB, and portions of areas 2 and 3 were outside the f-1 contour of WB. Much of WB's f-2 area overlapped the maximum wind area in Fig. 6 and Fujita's area 4. Wind swath values in Fig. 7 were compared with equivalent sustained wind speeds (shown in the key of Fig. 8) derived from the f contours in Fig. 8. The f-1 contours between Coral Gables and Kendall, and south of Homestead, represent F-2 maximum 1-min winds of 45 m s^{-1} and compare to analysis wind speeds of 45–60 m s^{-1} between Coral Gables and Kendall, and 55 m s^{-1} south of Homestead. In Perrine, the f-2 contour represents F-3.0 winds of 61 m s^{-1} compared to maximum analysis wind speeds of 62 m s^{-1}. In the Naranja Lakes area, the f-3 contour represents F-3.5 winds 23% higher than the analysis maximum wind swath (69 m s^{-1} compared to swath winds of 56 m s^{-1}).

In general, the revised f scale compares better with the Andrew analysis wind field than the original F scale compared with the Hurricane Frederic wind field. Damage analyses suggesting wind speeds higher than those analyzed in the vicinity of Naranja Lakes (Fujita and WB) may be overestimated because of a construction flaw [failure to tie down the roof to the walls and foundation (Zollo 1993)]. In the Homestead–Florida City areas 2 and 5, Fujita's analysis shows numerous f-2 damages suggesting winds greater than those indicated in the maximum V_{M1} swath in Fig. 7.

d. Crandell's damage survey

The engineering damage survey by Crandell (1993) consisted of inspections of nearly 500 homes located in nine street grids (labeled A–I in Fig. 8) chosen randomly from the damage area. The inspections categorized damage according to uniform construction details; construction and design details control the survivability of a structure and must be a primary consideration when evaluating damage. For example, Crandell (1993) found that hip roofs performed better than gable roofs and that one-story homes with gable roofs performed better than two-story versions.

Crandell (1993) studied the severity of damage to one-story homes with gable roofs in grids A–I of Fig. 8 by assigning a peak wind speed (from an earlier version of Fig. 7) to each of the areas. Grids A and B experienced V_{M1} wind speeds greater than 50 m s^{-1} for about 1.4 h compared with about 0.75 h at grids G–I. Grids A and B of Fig. 8 were assigned to a high-wind category, and grids G–I to a lower-wind category. Contrary to expectations, Crandell found 76% of the homes in the lower-wind category experienced severe roof damage compared with 48% in the higher-wind category. These results are in agreement with the findings of Fujita (1992a) in the vicinity of Homestead–Florida City, where f-2 damage suggested winds greater than those analyzed. Another possible explanation for the differences in damage relative to the peak sustained wind areas may be that the locations with higher damage received higher winds in small-scale downdrafts associated with convective cells identified in the radar animations; the wind analyses described here depend heavily on adjusted flight-level observations that did not sample such features. The lack of agreement between peak winds and damage in these areas points out the limitations of using a peak wind alone to estimate damage; other factors come into play, such as duration of strong winds, structural sensitivity to wind direction, local topographic effects, and subgrid-scale convective downdrafts or microbursts.

The greater damage at grids G–I may be related to the range of wind directions experienced while winds were greater than 50 m s^{-1} (or some other threshold). While winds were greater than 50 m s^{-1}, the wind field analyses indicate that locations A and B experienced a 90° wind direction change, while grids G–I received direction shifts of 165° and 150°, respectively. Crandell (1993) reported that roof failures are associated with large suction pressures that develop in localized areas (such as eaves, overhangs, and building corners) of the structure relative to the wind direction. Therefore, if a home is subject to a large variation of wind direction during high winds, there is a better chance of experiencing a direction for which the design, geometry, and construction of the home is susceptible.

6. Real-time applications

According to a policy statement on hurricane detection, tracking, and forecasting issued by the American Meteorological Society (AMS 1993), the major hazards of a hurricane are the storm surge, flooding from heavy rain, strong winds, and hurricane-spawned tornadoes. Storm surge has historically been responsible for the largest loss of life and damage; losses from flooding typically occur well inland, long after the hurricane has dissipated. Wind damage is usually not as catastrophic as storm surge but can affect a much larger area. Hurricane evacuation plans consider the threat of storm surge, but it is not practical to evacuate for wind; many people must survive strong winds in their homes. Detailed information on the severity and extent of the winds affecting these people is needed by forecasters and emergency managers.

While the benefits of improvements in forecast and warning accuracy over the past two decades have undoubtedly saved lives and property (Sheets 1990), firsthand experience with Andrew has identified the potential for additional uses of information during and immediately after hurricane disasters. Griffin et al. (1992) have developed techniques for airborne analysis of radar reflectivity and Doppler wind measurements for real-time transmission to forecasters at the National Hurricane Center. Other developments nearing completion include transmission of three-dimensional airborne Doppler wind fields above the boundary layer (Roux et al. 1991) and remotely sensed surface wind speed and direction measurements (Tanner et al. 1987; Black et al. 1995). As a result of improvements in the dissemination of information over networks and distributed computing, it is now possible to perform real-time analysis of hurricane wind fields. The first real-time objective analyses of hurricane surface wind fields were completed in Hurricane Emily of 1993 (Burpee et al. 1994).

Advances in Geographical Information System (GIS) technology make it possible to combine real-time meteorological fields with infrastructure and demographics databases to allow emergency managers to assess the impact of a major hurricane during landfall. In addition to wind, storm surge height predictions and radar reflectivity fields are primary candidates for use in GIS applications. These fields must be interpreted carefully. The highest sustained wind speeds or peak radar reflectivity values may not correlate perfectly with the most severe damage; they will however, provide a coarse view of the areas most affected by the storm.

a. Warnings and emergency management

The product most useful to forecasters up to the time of landfall is the V_{M1} field. The example in Fig. 9 provides useful information on the radii of 18 m s^{-1} (gale force), 25 m s^{-1}, and 33 m s^{-1} (hurricane force) winds (also see Fig. 3c) required for public advisories. Once the landfall position has been determined, a wind swath field similar to Fig. 7 can be generated for the immediate landfall area by projecting the wind field along the current storm track. Release of this information to emergency managers with GIS will allow linkage to detailed maps and demographics databases for assessment of the disaster impact in terms of the number of people affected and the amount of supplies required for assistance. To evaluate the wind threat farther inland, a decay model may be applied based on input parameters determined from the analysis wind field at landfall. Kaplan and DeMaria (1995) have con-

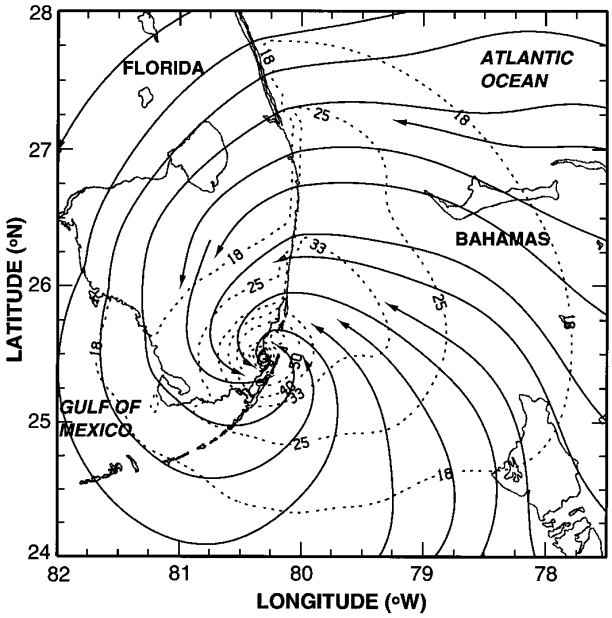

FIG. 9. Merged V_{M1} (m s^{-1}) analysis as in Fig. 3c but for mesh 4.

structed a model that creates a decaying wind field over land based on parameters determined from the observed wind field for oceanic exposure at landfall. A preliminary example of this type of product applied to Hurricane Andrew (mesh 4) is presented in Fig. 10, based on initial input parameters from the oceanic exposure V_{M1} analysis. On the west side of the wind swath the modeled decay of the wind field over land compares well with the observed decay (Fig. 6) in the core region. On the east side, however, the model has difficulty fitting the observed land–sea asymmetry into the wind field, and winds are underestimated to the left of the track. Forecasts of the decaying wind field presented relative to the official forecast track will help forecasters to estimate the potential inland hazard of strong winds.

b. Storm surge and wave model simulations

Based on comparisons of observed and modeled wind fields in Tropical Storm Marco, Houston and Powell (1994) advocated using real-time wind field analyses to provide input to the Sea, Lake, and Overland Surge from Hurricanes (SLOSH) model (Jelesnianski et al. 1992). For real-time wind field input to storm surge and wave models, the maximum 10-min mean surface winds (V_{M10}) are considered to be more representative of timescales associated with ocean response to surface stress than V_{M1}. Furthermore, the SLOSH model is driven by winds that are considered to be equivalent to 10-min averages. The V_{M10} field may be computed from the mesoscale analysis according to

$$V_{M10} = V_{meso}(G_{600,T_m}), \quad (4)$$

where G_{600,T_m} is the gust factor for the maximum 10-min wind that might occur over some longer mesoscale time period. A relationship for G_{600,T_m} was developed with National Oceanic and Atmospheric Administration (NOAA) C-MAN station data collected in tropical cyclones from 1985 to 1991. The maximum 10-min wind computed in this manner over a T_m of 1 h would represent nearly one standard deviation in a normal probability plot with a <33% chance of that location experiencing a higher V_{M10} over the hour.

The peak high-water marks surveyed after Andrew are displayed with the V_{M10} field in Fig. 11 for 0830 UTC 24 August 1992. The SLOSH wind field generated for a hurricane moving at 8 m s^{-1} (with an R_{MAX} of 14.5 km and a pressure difference of 8.7 kPa between the eye and the periphery) is displayed for the same time period in Fig. 12, together with the model-predicted high-water marks (storm surge plus tide). The SLOSH model computes ''lake winds'' over bays and inland lakes to take land-exposure influences into account. Lake winds within Biscayne Bay have slightly more inflow and weaker speeds than the oceanic SLOSH winds farther offshore. The peak SLOSH winds on the north side of the eye are close to the same as the analysis winds but cover a much larger portion of the eyewall and are located closer to the storm center. The peak SLOSH winds near the southern eyewall

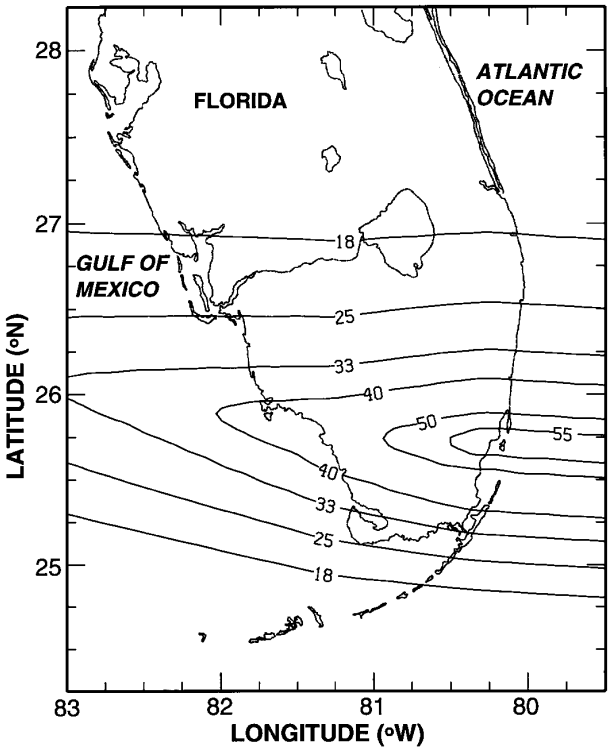

FIG. 10. DeMaria–Kaplan decay model wind swath field for mesh 4. Winds are only valid over land and over water east of the Florida Atlantic coast.

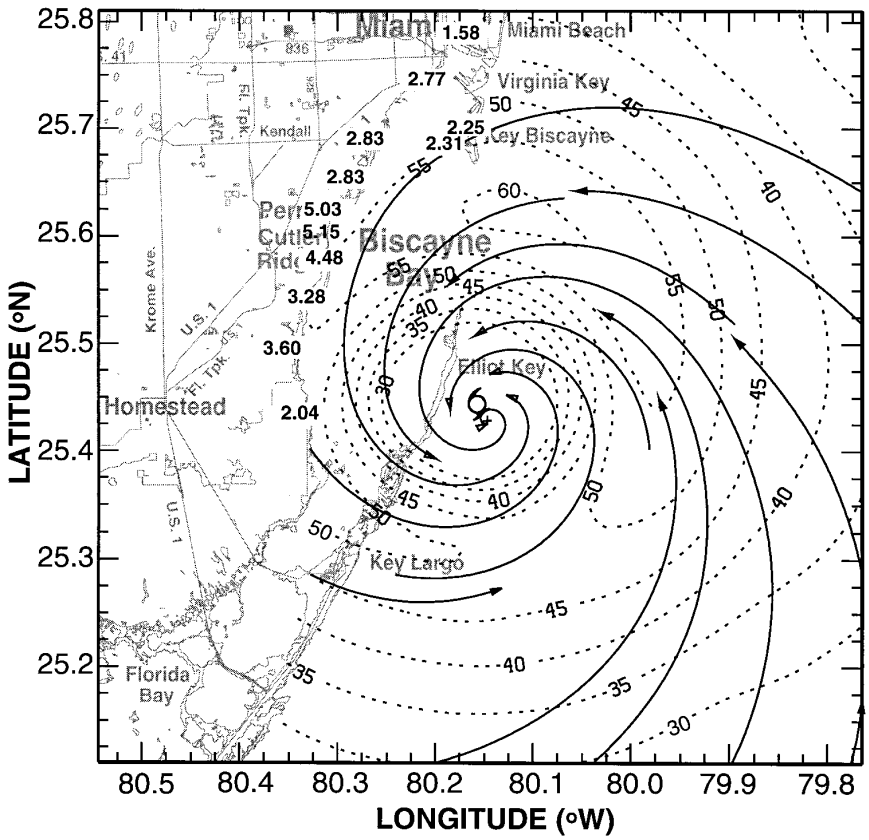

FIG. 11. The V_{M10} (m s^{-1}) analysis (over water exposure) and poststorm high-water mark measurements (*m*) for mesh 1 at 0830 UTC 24 August 1992.

are about 10 m s^{-1} larger than the analysis wind field. In general, the SLOSH high-water values are 1–1.5 m higher than the measured values except in the region of the peak value, where SLOSH slightly underpredicted the peak.

If real-time wind field analyses become available on a regular basis, a storm surge model could be run based on input from actual wind field measurements. Analysis fields are needed because wind field model simulations are vulnerable when applied to storms with asymmetric wind fields, such as Hurricane Emily in 1993. Emily's peak winds were nearly the same strength on the west and east sides of the northward moving storm during its closest approach to Cape Hatteras (Burpee et al. 1994), resulting in higher than expected storm surge caused by offshore flow from Pamlico Sound (Pasch and Rappaport 1995). Real-time analysis wind fields may also be used to compute refined surge height values once the landfall point is known. This field would provide a preliminary assessment of the areas actually inundated by the surge. Emergency managers would have available both the V_{M1} and the storm surge fields for use with GIS to assist decision making while the storm is still in progress.

Hurricane wind fields also generate waves that can threaten ocean commerce from long distances. Wave forecasts are necessary to warn marine interests and evacuate personnel from offshore structures. Wave models such as the third-generation WAM (WAMDI Group 1988) are being employed for operational wave prediction using input surface stress fields derived from operational surface wind analyses of marine observations from ships and buoys largely in conformance with the World Meteorological Organization recommendation of a 10-min mean wind sampling period. Jensen et al. (1993) showed that analyses of V_{M10} wind fields from the Halloween Storm of 1991 could produce accurate hindcasts when used as input to WAM. Analyses of V_{M10} in hurricanes, when blended with oceanic wind fields from numerical forecast models and remotely sensed satellite winds from data-poor areas far from the storm, may have potential for real-time input to wave models.

c. Peak gusts and the design wind

Wind engineers, designers, and interests in the construction and insurance industry require timely wind field information to establish the recurrence interval for

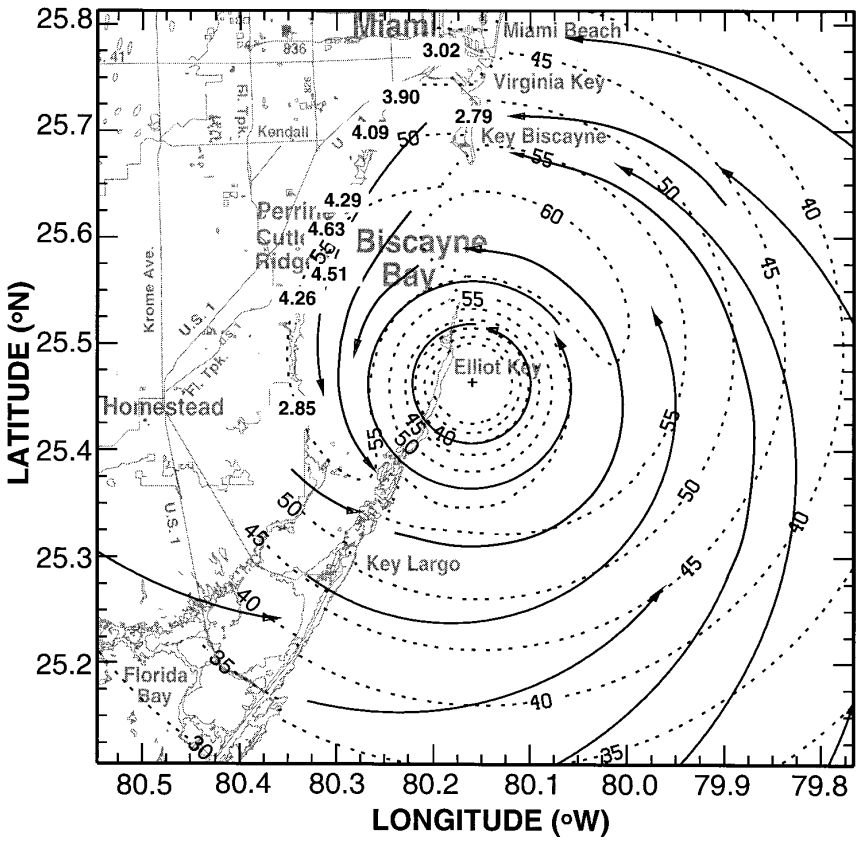

FIG. 12. As in Fig. 11 but for SLOSH parametric wind model and SLOSH-predicted high-water marks (*m*).

the peak wind and whether design winds (the winds used to compute wind loads on structures) were exceeded. In the past, discussions of peak winds in hurricanes suffered from the lack of a standard terminology. For example, wind engineers would discuss ''fastest mile'' winds (the wind speed corresponding to the fastest movement of a 1-mile-long ribbon of air past an anemometer), while meteorologists would refer to V_{M1}. Fastest mile wind speeds are being discontinued in revised wind load standards; the national wind load standard (ASCE 1994) adopted for the building code of Dade County references design winds as peak 3-s gusts (V_{G3}) (H. Saffir 1994, personal communication). Dividing the gust factor for the peak V_{G3} over 1 h [$G_{3,3600}$ = 1.67, Krayer and Marshall (1992)] by the gust factor for the peak V_{M1} over 1 h [averaging the Durst (1960) value of 1.24 and Krayer and Marshall's value of 1.33 yields $G_{60,3600}$ = 1.28] results in the peak 3-s gust during the peak V_{M1} of 1.3 V_{M1}. Hence, over 1 h the peak 3-s gust over land is approximately 30% higher than V_{M1}. Over water, V_{G3} is not as large relative to V_{M1} because of reduced turbulence there. Rather than peak 3-s gusts, automated buoys and C-MAN platforms measure peak 5-s gusts; there is very little difference between the peak 3- and 5-s gust over some longer period. Based on the Hurricane Bob Coastal Engineering Research Center data (see Part I) and 147 C-MAN wind measurements in tropical cyclones, $G_{5,60}$ = 1.13 was computed as an oceanic gust factor. The V_{M1} swath of Fig. 7 was converted to V_{G3} over land and V_{G5} over water and is depicted in Fig. 13. The gust swath map will help to establish whether design winds were exceeded for coastal, inland, and offshore structures and minimize confusion among various disciplines when referring to the peak winds caused by the storm.

d. Damage assessment and disaster mitigation

The ultimate cost of a disaster is related to the amount of time taken for a community to recover; a faster, more organized recovery will help to mitigate the losses associated with a storm. Real-time information on the actual areas impacted by the eyewall and the strongest winds would help minimize confusion and assist recovery management at the earliest stages of the disaster. The ability of GIS to link meteorological field information to damage statistics from infrastructure databases makes damage assessment modeling a possi-

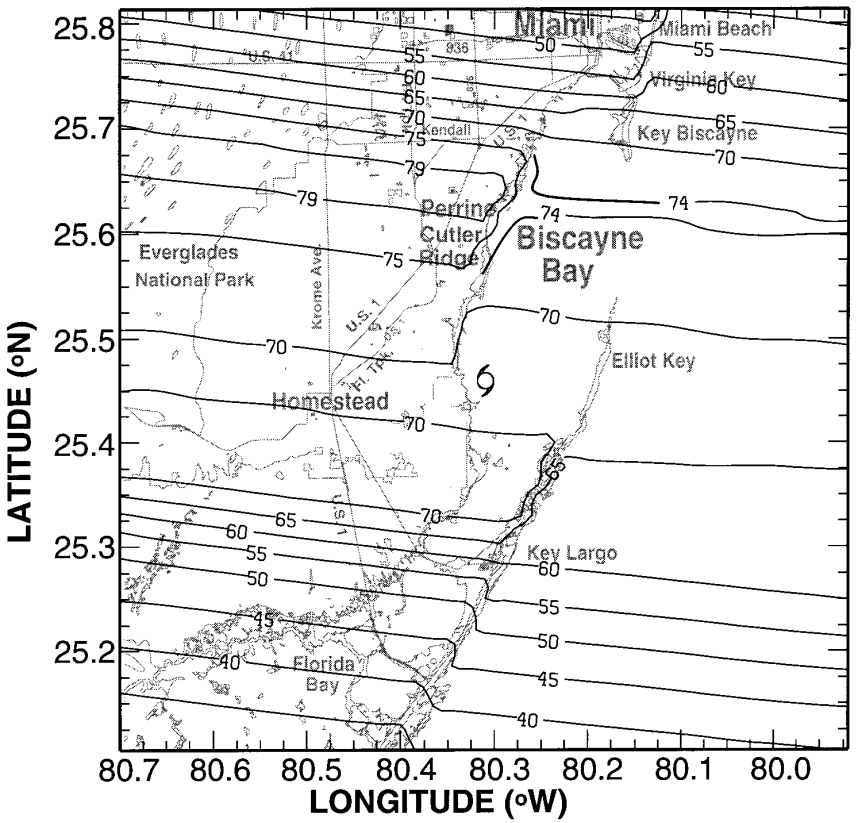

FIG. 13. Swath map for peak 3-s gust, V_{G3} (m s^{-1}), over land and peak 5-s gust (V_{G5}) over water.

bility. An example of the use of GIS in disaster recovery planning is illustrated by an overlay (Fig. 14) of the Andrew V_{M1} swath on a map showing Florida Power and Light Company (FP&L) electrical utility substations in the Princeton area between Perrine and Homestead. The area shown on the map is identified as an inset dashed box in Fig. 7. The irregular polygon in Fig. 14 corresponds to the Princeton Storm Headquarters area where reports of damage to FP&L facilities within the area were compiled during the recovery process. The area weighted peak V_{M1} for the polygon is 57.4 m s^{-1}. If georeferenced statistics on the damaged facilities of each substation were available for categories of uniform structures (support poles, conductors, transformers), it would be possible to correlate losses with quantities derived from meteorological fields believed to be associated with damage. Candidate fields could be screened to create a multiple regression model for percentage damage to a particular type of structure within a specified area on a geographic grid. We are currently attempting to create such a model in cooperation with engineers from FP&L. Unfortunately, damage databases of this nature are not easily available. Reestablishing infrastructure services after a major disaster consumes resources that might be used to evaluate damage at a substation-scale resolution; data are often only available for geographic areas that are too large to correlate with high-resolution meteorological fields. We have identified a few areas impacted by Hurricane Andrew that are small enough to be candidates for correlating damage to a variety of structures relevant to the electrical power infrastructure with quantities determined from the wind and reflectivity fields; this work is ongoing. If successful, the availability of such models would permit real-time assessment of damage. Beyond the electrical utility industry, other segments of the infrastructure could benefit from a similar approach. With models available for all segments of the infrastructure, a preliminary indication of the impact of the disaster would be possible while the storm is in progress or immediately afterward instead of days later, after visual assessments are completed. Scenarios for the impact of hurricanes on a community could also be created by applying the damage model to a historical or model-simulated wind field and a given radar reflectivity structure.

7. Conclusions

We have analyzed all available wind data collected from Hurricane Andrew's passage across Florida. All

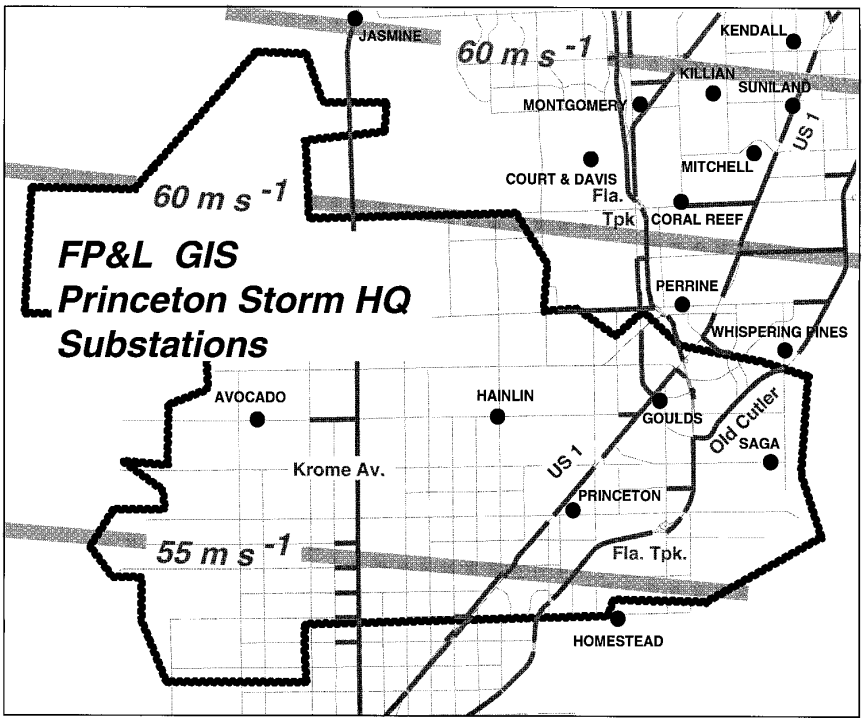

FIG. 14. GIS overlay of maximum V_{M1} swath (m s^{-1}) from Hurricane Andrew with locations (filled circles) and names of Florida Power and Light Corporation electrical power substations in the Princeton storm headquarters area. Location of box is shown as an inset to Fig. 7.

data were carefully quality controlled and processed to correspond to a common framework consisting of maximum 1-min sustained winds at the 10-m level for open terrain over land or for oceanic exposure over sea. At landfall (0900 UTC 24 August), maximum V_{M1} winds of 66 m s^{-1} associated with the northern eyewall were found on the Biscayne Bay coastline in the vicinity of Perrine. These winds decreased to 62 m s^{-1} just inland from the coast. Enhanced convergence was observed along the coastline to the north of the center (where onshore flow was decelerated by the terrain), and divergence was noted to the south of the center where flow accelerated offshore. Animation of radar reflectivity images from the MLB and TBW radars could not substantiate whether convective cells were enhanced by coastline convergence. The V_{M1} field, length scales of intense damage swaths, and the amplitude of the analyzed eyewall-scale vorticity field suggest that streak vortices or miniswirls hypothesized by Fujita may be produced by cyclonic horizontal shear on the edges of downdraft gusts on the inner edge of the eyewall wind maximum. Convergence and associated lifting at the head of a downdraft could rapidly increase vorticity through stretching in a manner similar to that hypothesized for gustnadoes.

During Andrew's transit of the Florida peninsula, the peak V_{M1} over land decreased by 33% to 44 m s^{-1}. Most of the decrease in the wind field occurred in the core of the storm; winds changed little at distances 50–60 km from the center. The exit divergence pattern was reversed; a convergence zone associated with onshore flow was located to the south of the center, in agreement with convective cell development seen in radar animations from MLB and TBW. The observed 9-K decrease of equivalent potential temperature in the eye suggests that, as with Hurricane Donna in 1960, Andrew weakened due to loss of its oceanic heat source despite traveling over the relatively moist Everglades.

A swath of maximum V_{M1} was compared with two Fujita-scale surveys and an engineering damage survey. The swath of maximum V_{M1} diagnosed from the wind analyses compared well with portions of both Fujita-scale surveys. Based on conversions of the f scale to V_{M1} equivalents, the most severe f-3 damage was found in areas where the V_{M1} swath indicated F-3 winds. However, the locations of f-2 damage in the surveys also corresponded to V_{M1} swath winds of F-3. Comparisons with randomly chosen grids of single-story, gable roof homes in nine damage areas suggest that V_{M1} alone may not necessarily correlate best with damage. Given the directional susceptibility of roofs to intense suction pressures at corners and overhangs, an important consideration is the amount of wind direction change during high winds over some threshold velocity.

Andrew's landfall and the immediate recovery problems have underscored the importance of providing real-time hurricane wind and reflectivity structure information to forecasters, emergency managers, and infrastructure concerns. In the future, the availability of dense prelandfall reconnaissance and research aircraft flight-level wind measurements and coastal, offshore, and inland observations will allow real-time surface wind analyses to be completed in a storm-relative coordinate framework. When combined with high-resolution GIS and infrastructure databases, these fields will be valuable to emergency managers and infrastructure concerns for identification of the hardest hit areas. In addition, real-time wind field information may also be used to improve storm surge and wave model forecasts. To progress further, an experience base must be developed from several storms in which quantities derived from meteorological fields may be correlated with damage statistics from various parts of the infrastructure. This base will eventually lead to the construction of models capable of rapid and accurate damage assessment.

Acknowledgments. This study was supported by the Coastal Hazards component of the NOAA Coastal Ocean Program and Research Grant 93MGD03 from Florida Power and Light Company. The authors would like to thank Dr. Peter Black of HRD for information on the Fujita-scale surveys and Brian Jarvinen of NHC for supplying information on the distribution of storm surge. Special thanks go to James Franklin, Sim Aberson, and Steve Feuer for their guidance in applying HRD's nested SAFER analysis techniques to surface winds; to Robert Kohler and Cary Bakker for developing software for displaying the wind fields; to Neal Dorst and Gus Pujals for assistance in contructing base maps; to Peter Dodge for creating loops of imagery from the Melbourne WSR-88D radar; and to John Kaplan and Dr. Mark DeMaria for supplying the wind field decay model computations. The manuscript benefited from reviews by Dr. Robert Burpee, Michael Black, Chris Samsury, and Vic Wiggert of HRD; Dr. Wilson Shaffer of the NWS Techniques Development Laboratory; Dr. Ed Rappaport of NHC; Jeff Keppert of the Australian Bureau of Meteorology Research Center; and anonymous reviewers.

REFERENCES

AMS, 1993: Policy statement: Hurricane detection, tracking, and forecasting. *Bull. Amer. Meteor. Soc.,* **74,** 1377–1380.

Anthes, R. A., 1982: *Tropical Cyclones. Their Evolution, Structure and Effects, Meteor. Monogr.,* No. 41, Amer. Meteor. Soc., 208 pp.

ASCE, 1994: Minimum design loads for buildings and other structures. ASCE 7-93, American Society of Civil Engineers, 134 pp. [Available from ASCE Publications Office, 345 E 47th Street, New York, NY 10017-2398.]

Black, P., R. McIntosh, C. Swift, J. Carswell, K. St. Germain, I. Popstefanija, and M. Goodberlet, 1995: Ocean surface wind, stress and rain rate measurements in tropical cyclones from concurrent airborne microwave scatterometer and radiometer observations. Preprints, *27th Conf. on Radar Meteorology,* Vail, CO, Amer. Meteor. Soc., 623–625.

Burpee, R. W., and Coauthors, 1994: Real-time guidance provided by NOAA's Hurricane Research Division to forecasters during Emily of 1993. *Bull. Amer. Meteor. Soc.,* **75,** 1765–1783.

Crandell, J. H., 1993: Assessment of damage to single-family homes caused by Hurricanes Andrew and Iniki. HUD-PD&R-1432, 127 pp. [Available from U.S. Dept. of Housing and Urban Development, Washington, DC 20410-6000.]

DeMaria, M., S. M. Aberson, K. V. Ooyama, and S. J. Lord, 1992: A nested spectral model for hurricane track forecasting. *Mon. Wea. Rev.,* **120,** 1628–1643.

Dodge, P., M. Black, P. Leighton, B. Cristoe, F. D. Marks Jr., and R. Burpee, 1993: Time-lapse radar images of Hurricane Andrew's landfalls. Preprints, *20th Conf. on Hurricanes and Tropical Meteorology,* San Antonio, TX, Amer. Meteor. Soc., 163–166.

Doswell, C. A., III, and D. W. Burgess, 1988: On some issues of United States tornado climatology. *Mon. Wea. Rev.,* **116,** 495–501.

Durst, C. S., 1960: Wind speeds over short periods of time. *Meteor. Mag.,* **89,** 181–186.

Fletcher, R. D., J. R. Smith, and R. C. Bundgaard, 1961: Superior photographic reconnaissance of tropical cyclones. *Weatherwise,* **14,** 102–109.

Forbes, G. S., and R. M. Wakimoto, 1983: A concentrated outbreak of tornadoes, downbursts and microbursts, and implications regarding vortex classification. *Mon. Wea. Rev.,* **111,** 220–235.

Franklin, J. L., S. J. Lord, and F. D. Marks Jr., 1988: Dropwindsonde and radar observations of the eye of Hurricane Gloria (1985). *Mon. Wea. Rev.,* **116,** 1237–1244.

——, ——, S. E. Feuer, and F. D. Marks, 1993: The kinematic structure of Hurricane Gloria (1985) determined from nested analyses of dropwindsonde and Doppler data. *Mon. Wea. Rev.,* **121,** 2433–2451.

Fujita, T. T., 1971: Proposed characterization of tornados and hurricanes by area and intensity. SMRP Research Paper 91, Dept. of Geophys. Sci., University of Chicago, 42 pp.

——, 1992a: Damage survey of Hurricane Andrew in south Florida. *Storm Data,* **34,** 25–30. [Available from NOAA/National Climatic Data Center, Federal Building, 151 Patton Avenue, Asheville, NC 28801-5001.]

——, 1992b: *Mystery of Severe Storms.* 298 pp. [Available from Wind Research Laboratory, Dept. of Geophysical Sciences, 5734 Ellis Ave., Chicago, IL 60637.]

Griffin, J. S., R. W. Burpee, F. D. Marks Jr., and J. L. Franklin, 1992: Real-time airborne analysis of aircraft data supporting operational hurricane forecasting. *Wea. Forecasting,* **7,** 480–490.

Houston, S. H., and M. D. Powell, 1994: Observed and modeled water level response from Tropical Storm Marco (1990). *Wea. Forecasting,* **9,** 427–439.

Jensen, R. E., S. H. Houston, C. L. Vincent, and M. D. Powell, 1993: Evaluation of a third generation wave model for the U.S. Atlantic coast. *Ocean Wave Measurement and Analysis, Proc. Second Int. Symp.,* New Orleans, LA, ASCE, 433–447.

Jeslesnianski, C. P., J. Chen, and W. A. Shaffer, 1992: SLOSH: Sea, lake, and overland surges from hurricanes. NOAA Tech. Rep. NWS 48, Silver Spring, MD, 71 pp. [Available from Techniques Development Lab-NWS, 1325 East–West Highway, Silver Spring, MD 20910.]

Jordan, C. L., 1961: Marked changes in the characteristics of the eye of intense typhoons between the deepening and filling stages. *J. Meteor.,* **18,** 779–789.

Jorgensen, D. P., E. J. Zipser, and M. A. LeMone, 1985: Vertical motions in intense hurricanes. *J. Atmos. Sci.,* **42,** 839–856.

Kaplan, J., and M. DeMaria, 1995: A simple empirical model for predicting the decay of tropical cyclone wind fields after landfall. *J. Appl. Meteor.,* **34,** 2499–2512.

Krayer, W. R., and R. D. Marshall, 1992: Gust factors applied to hurricane winds. *Bull. Amer. Meteor. Soc.,* **73,** 613–617.

Lord, S. J., and J. L. Franklin, 1987: The environment of Hurricane Debby. Part I: Winds. *Mon. Wea. Rev.,* **115,** 2760–2780.

Malkus, J. S., and H. Riehl, 1960: On the dynamics and energy transformations in steady-state hurricanes. *Tellus,* **12,** 1–20.

Mayfield, M., L. A. Avila, and E. N. Rappaport, 1994: The Atlantic hurricane season of 1992. *Mon. Wea. Rev.,* **122,** 517–538.

Miller, B. I., 1964: A study on the filling of Hurricane Donna (1960) over land. *Mon. Wea. Rev.,* **92,** 389–406.

Minor, J. E., J. R. McDonald, and K. C. Mehta, 1977: Engineering oriented examinations of the tornado phenomenon. Preprints, *10th Conf. on Severe Local Storms,* Omaha, NE, Amer. Meteor. Soc., 438–445.

Ooyama, K. V., 1987: Scale-controlled objective analysis. *Mon. Wea. Rev.,* **115,** 2479–2506.

Parrish, J. R., R. W. Burpee, F. D. Marks Jr., and R. Grebe, 1982: Rainfall patterns observed by digitized radar during the landfall of Hurricane Frederic (1979). *Mon. Wea. Rev.,* **110,** 1933–1944.

Pasch, R. J., and E. N. Rappaport, 1995: Atlantic hurricane season of 1993. *Mon. Wea. Rev.,* **123,** 871–886.

Powell, M. D., 1982: The transition of the Hurricane Frederic boundary layer wind field from the open Gulf of Mexico to landfall. *Mon. Wea. Rev.,* **110,** 1912–1932.

——, 1987: Changes in the low-level kinematic and thermodynamic structure of Hurricane Alicia (1983) at landfall. *Mon. Wea. Rev.,* **115,** 75–99.

——, P. P. Dodge, and M. L. Black, 1991: The landfall of Hurricane Hugo in the Carolinas: Surface wind distribution. *Wea. Forecasting,* **6,** 379–399.

——, S. H. Houston, and T. Reinhold, 1996: Hurricane Andrew's landfall in south Florida. Part I: Standardizing measurements for documentation of surface wind fields. *Wea. Forecasting,* **11,** 304–328.

Rappaport, E. N., 1994: Hurricane Andrew. *Weather,* **49,** 51–61.

Roux, F., F. D. Marks Jr., and J. F. Gamache, 1991: Three-dimensional circulation in a hurricane from airborne Doppler radar data: Extended velocity track display. Preprints, *25th Int. Conf. on Radar Meteorology,* Paris, France, Amer. Meteor. Soc., 466–469.

Sheets, R. C., 1990: The National Hurricane Center—Past, present, and future. *Wea. Forecasting,* **5,** 185–232.

Simpson, R. H., and H. Riehl, 1981: *The Hurricane and Its Impact.* Louisiana State University Press, 398 pp.

Tanner, A., C. T. Swift, and P. G. Black, 1987: Operational airborne remote sensing of wind speeds in hurricanes. Extended Abstracts, *17th Conf. on Hurricanes and Tropical Meteorology,* Miami, FL, Amer. Meteor. Soc., 385–387.

Tuleya, R. E., 1994: Tropical storm development and decay: Sensitivity to surface boundary conditions. *Mon. Wea. Rev.,* **122,** 291–304.

——, and Y. Kurihara, 1978: A numerical simulation of the landfall of tropical cyclones. *J. Atmos. Sci.,* **35,** 242–257.

——, M. A. Bender, and Y. Kurihara, 1984: A simulation study of the landfall of tropical cyclones using a movable nested-mesh model. *Mon. Wea. Rev.,* **112,** 124–136.

Wakimoto, R. M., and P. G. Black, 1993: Damage survey of Hurricane Andrew and its relationship to the eyewall. *Bull. Amer. Meteor. Soc.,* **75,** 189–200. [Poster available from NOAA/HRD, 4301 Rickenbacker Cswy., Miami, FL 33149.]

WAMDI Group, 1988: The WAM model—A third-generation ocean wave prediction model. *J. Phys. Oceanogr.,* **18,** 1775–1810.

Willoughby, H. E., and P. G. Black, 1996: Hurricane Andrew in Florida: Dynamics of a disaster. *Bull. Amer. Meteor. Soc.,* **77,** 543–549.

——, J. M. Masters, and C. W. Landsea, 1989: A record sea level pressure observed in Hurricane Gilbert. *Mon. Wea. Rev.,* **117,** 2824–2828.

Wilson, J. W., 1986: Tornadogenesis by nonprecipitation induced wind shear lines. *Mon. Wea. Rev.,* **114,** 270–284.

Zollo, R. F., 1993: Hurricane Andrew: August 24, 1992: Structural performance of buildings in Dade County, Florida. Dept. of Civil and Architectural Engineering Tech. Rep. CEN 93-1, 69 pp. [Available from Department of Civil and Architectural Engineering, University of Miami, McArthur Bldg., Coral Gables, FL 33124.]